The fence experiment – full-scale lidar-based shelter observations

Alfredo Peña[1], Andreas Bechmann[1], Davide Conti[1], and Nikolas Angelou[1]
[1]DTU Wind Energy, Technical University of Denmark, Roskilde, DK
Correspondence to: Alfredo Peña (aldi@dtu.dk)

Abstract. We present shelter measurements of a fence from a field experiment in Denmark. The measurements were performed with three lidars scanning on a vertical plane downwind of the fence. Inflow conditions are based on sonic anemometer observations of a nearby mast. For fence-undisturbed conditions, the lidars' measurements agree well with those from the sonic anemometers and, at the mast position, the average inflow conditions are well described by the logarithmic profile. Seven cases are defined based on the relative wind direction to the fence, the fence porosity, and the inflow conditions. The larger the relative direction, the lower the effect of the shelter. For the case with the largest relative directions, no sheltering effect is observed in the far wake (distances $\gtrapprox 6$ fence heights downwind of the fence). When comparing a near-neutral to a stable case, a stronger shelter effect is noticed. The shelter is highest below ≈ 1.46 fence heights and can sometimes be observed at all downwind positions (up to 11 fence heights downwind). Below the fence height, the porous fence has a lower impact on the flow close to the fence compared to the solid fence. Velocity profiles in the far wake converge onto each other using the self-preserving forms from two-dimensional wake analysis.

1 Introduction

The flow around obstacles is difficult to observe and model because of the turbulence characteristics and velocity shears. Such flow has not received much attention in wind energy partly due to the urge to decrease the cost of energy, narrowing the research on flow characteristics to large-turbine operating conditions. These turbines generally operate in areas and at heights, where the obstacles' effects can be neglected. However, due to the decrease of available 'high wind' sites on land, turbines are being deployed in environments, where obstacles cannot be ignored. Also, the 'small' turbine industry has steadily grown (Gsänger and Pitteloud, 2014) and small machines are commonly installed close to obstacles. In Denmark, small turbines (< 25 kW) are normally placed closer than 20 m from buildings and below 25 m from the ground. Due to shelter, such installations often result in lower-than-expected yields and turbine breakdown.

Computational fluid dynamics (CFD) methods, e.g. those solving the Reynolds-averaged Navier-Stokes (RANS) equations, can accurately describe the flow around obstacles and are used to study specific flow conditions (Iaccarino et al., 2003). However, they are often too expensive to be implemented in wind-resource assessment tools. Therefore, the obstacles' effect is normally estimated using 'engineering'-like models. Some, e.g. WEMOD (Taylor and Salmon, 1993) and WAsP-shelter (Mortensen et al., 2007), are based on the analytical theory by Counihan et al. (1974), which describes the wake behind two-dimensional (2D) obstacles, and consider wakes behind three-dimensional (3D) objects.

Analytical theories and CFD simulations have mainly been evaluated with wind-tunnel data (Castro and Robins, 1977) and few full-scale 3D shelter experiments have been performed. Nägeli (1953) is perhaps the first to investigate the mean velocity profiles downwind of porous windbreaks, although his data are not of the highest quality (Seginer, 1972). Most shelter experiments are associated with agro-engineering studies, where the purpose is windbreak optimization for stock and crop protection, and are focused on porous obstacles (Nord, 1991). Wilson (2004) describes a field experiment where the shelter of a 1.25-m high and 114-m wide porous plastic fence was measured as a function of the 'obliquity' of the inflow; the fence seems to have an effect on the flow for all the measurement positions (and all obliquities) along a transect that extends 20 fence heights at a vertical level about half the fence height. Shelter effects in oblique flows are studied by numerical simulations in Wang and Takle (1996). A review on modeling and simulation studies of windbreaks that includes comparison with experimental data is presented by Wang et al. (2001).

Here, we present a comprehensive dataset of full-scale measurements of a fence shelter. The measurements were conducted at Risø's test site in Denmark and the WindScanner (WS) lidar-based system was used to measure the 3D wind vector on a vertical plane for different inflow conditions. The experiment is somewhat similar to that of Wilson (2004) but we concentrated our measurement efforts close to the fence (both horizontally and vertically). The experiment's objective is to serve as benchmark for shelter models. Section 2 introduces the definitions and theory used to analyze the measurements. Section 3 provides details of the site and the measurements, Sect. 4 describes the way data are analyzed, and Sect. 5 presents the shelter results for a number of inflow conditions/cases. Finally, Sect. 6 provides some discussion and conclusions about the campaign and future model evaluation.

2 Definitions

2.1 Problem

We describe the turbulent flow behind a 2D fence (Fig. 1) and compare it to the undisturbed inflow (subscript $_o$). We use a right-handed Cartesian coordinate system with the three velocity components, u, v, and w, aligned with the x, y, and z (the vertical) axes, respectively. The horizontal wind-speed magnitude is thus $U = \left(u^2 + v^2\right)^{1/2}$. The coordinate center is placed on the ground at the fence. The flow is described by the roughness length z_o and the fence height h.

We investigate the flow on a 2D vertical plane extending $2.5\ h$ vertically and $\approx 11\ h$ horizontally downstream of the fence. For simplicity, two main regions are defined in this plane: the 'near-wake' ($x < 6\ h$) and the 'far-wake' ($x > 6\ h$) regions. In the analysis below, we describe the flow for different inflow directions and that perpendicular to the fence (along the x-axis).

2.2 Inflow

We assume that the inflow can be described by the diabatic wind profile (Stull, 1988),

$$U_o(z) = \frac{u_*}{\kappa}\left[\ln\left(\frac{z}{z_o}\right) - \psi_m(z/L)\right], \tag{1}$$

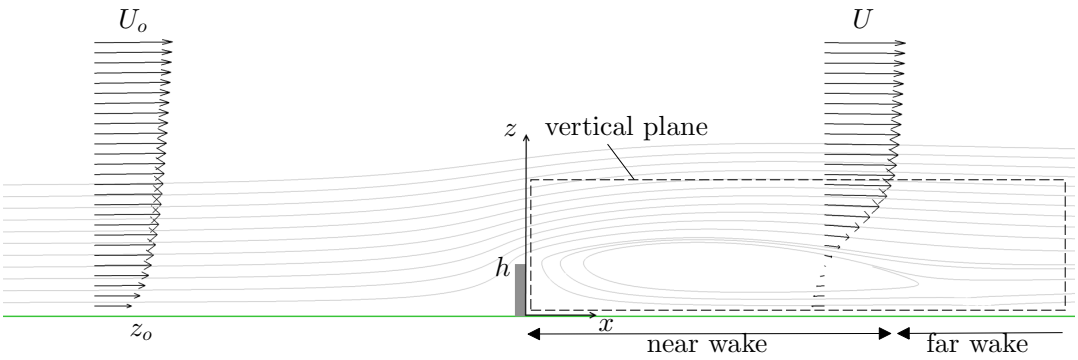

Figure 1. Simulated turbulent flow around a 2D fence of height h and the vertical plane of interest. The flow is simulated with the model described in Sect. 3.3.1

where u_* is the friction velocity, κ the von Kármán constant (≈0.4), and ψ_m a function of the dimensionless stability parameter z/L, being L the Obukhov length. u_* and L can be computed as

$$u_* = \left(\overline{u'w'}^2 + \overline{v'w'}^2\right)^{1/4}, \tag{2}$$

$$L = -\frac{{u_*}^3}{\kappa(g/\overline{T})\overline{w'\Theta'_v}}, \tag{3}$$

where g is the gravitational acceleration, T a reference temperature, Θ_v the virtual potential temperature, the primes denote fluctuations around the time average, and the overbar a time average.

2.3 Two-dimensional wake theory

The wind-speed ratio U/U_o at a specific height z is used to quantify the shelter and can be written as

$$\frac{U(x,z)}{U_o(z)} = 1 - \frac{\Delta U(x,z)}{U_o(h)}\,\frac{U_o(h)}{U_o(z)}, \tag{4}$$

where $\Delta U(x,z) = U_o(z) - U(x,z)$. The term $\Delta U(x,z)/U_o(h)$ is predicted by Counihans et al.'s analytical theory, in which a 2D obstacle wake is divided into three regions. Within the mixing region, spreading from the obstacle's top, the velocity is self-preserving with the form,

$$\frac{\Delta U(x,z)}{U_o(h)} = \frac{C/I(n)}{K\,h^2\,U_o(h)^2}\left(\frac{x}{h}\right)^{-1}\frac{d}{d\eta}\left[\eta^2\,{}_1F_1\left(\frac{2-n}{2+n}, \frac{n+4}{2+n}, \frac{-\eta^{n+2}}{(n+2)^2}\right)\right], \tag{5}$$

where C is related to the wake strength (see below), $K = 2\kappa^2/\ln(h/z_o)$, n the inflow's shear exponent, ${}_1F_1$ the confluent hypergeometric function, η a dimensionless length scale related to the mixing-region depth, and I an integral constant for the wake's self-preserving solution in the mixing region. The latter two are expressed as

$$I(n) = \frac{(1+n)(2+n)^{(4+n)/(2+n)}}{1+2n}\,\frac{\Gamma\left(\frac{4+n}{2+n}\right)\Gamma\left(\frac{1-n}{2+n}\right)}{\Gamma\left(\frac{2-n}{2+n}\right)}, \quad \text{and} \tag{6}$$

$$\eta = \left(\frac{z}{h}\right)\left[\frac{K\,x}{h}\right]^{-1/(n+2)}. \tag{7}$$

Counihan et al. shows that profiles of $\frac{\Delta U(x,z)}{U_o(h)}\left(\frac{x}{h}\right)$ as function of η converge onto each other within the far-wake region $6 \leq x/h \leq 30$ from full-scale measurements of the wind behind porous windbreaks and within the range $7.5 \leq x/h \leq 72$ from wind-tunnel measurements. Based on Counihan et al.'s theory and using wind-tunnel measurements behind 2D fences, Perera (1981) proposes an expression that has become the basis of engineering obstacle models,

$$\frac{\Delta U(x,z)}{U_o(h)} = A\,(1-\varphi)\left(\frac{x}{h}\right)^{-1}\eta\exp\left(-0.67\eta^{1.5}\right), \tag{8}$$

where φ is the fence porosity and A a constant ($= 9.75$).

The solution to the term $\frac{d}{d\eta}[...]$ in Eq. (5) is unattractive but for the special case $n = 0$, it is simple ($= 2\,\eta\exp\left(-0.25\eta^2\right)$). The self-similar profile $\frac{\Delta U(x,z)}{U_o(h)}\left(\frac{x}{h}\right)$ shows a maximum at $\eta(z/h \approx 1)$ and approaches zero with increasing η. For decreasing n values, the zero approach occurs at smaller η values and the profile's maximum slightly decreases (only 7% between $n = 0.14$ and 0). Also, I is not that sensitive to n ($= 7.64$ and 7.08 for $n = 0.14$ and 0, respectively). The expression $C = C_h\,h^2 U_o(h)^2$ is derived by Counihan et al. based on pressure measurements on blocks in shear flows from the Building Research Station Digest no. 119 (1970). Therefore, Eq. (5) can be simplified to

$$\frac{\Delta U(x,z)}{U_o(h)} = \frac{C_h}{K\,I(n=0.14)}\left(\frac{x}{h}\right)^{-1} 2\,\eta\exp\left(-0.25\eta^2\right). \tag{9}$$

Counihan et al. chooses $C_h = 0.8$ for measurements behind 2D blocks. Following the analysis by Taylor and Salmon (1993), C_h corresponds to the wake-moment coefficient. They suggest $C_h = B(1-\varphi)$ with $0.2 \leq B \leq 0.8$ depending on the obstacle type.

3 Site and measurements

We aim at describing the effect of a full-scale obstacle on the atmosphere by measuring on a vertical plane downwind of a fence. Here, we first describe the site, the inflow conditions from mast measurements, and the shelter measurements performed by the WS.

3.1 Site

The 'fence experiment' took place at Risø's test site, which is ≈7 km north from Roskilde and ≈35 km west from Copenhagen, Denmark (Fig. 2). It was conducted during two periods: from March 10 to April 1 the fence was solid and from September 29 to October 2 2015 the fence was made porous. The terrain at the site is slightly hilly and the surface is characterized as a mix between cropland, grassland, artificial land, and coast.

The fence is made of horizontal wooden panels with wooden beams on each side supporting the structure (see Fig. 3-bottom frames). For the second period of the experiment, the fence porosity (ratio of the 'pores' to the total area) is 0.375. The fence

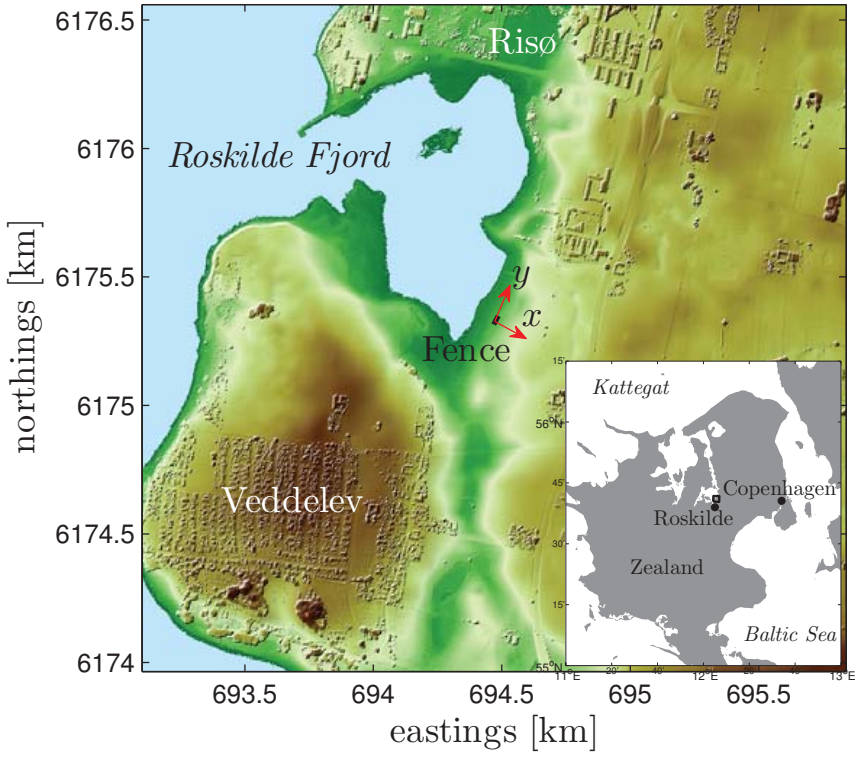

Figure 2. The fence experiment on a digital surface model (UTM32 WGS84) of the area surrounding Risø's test station. Cropland and grassland are shown in green, cropland and artificial land in light brown, rural areas and buildings in brown, and the waters from the fjord in light blue. The reference coordinate system is shown in red. In the bottom-right part, the test site location (black rectangle) on the island of Zealand, Denmark, is illustrated

is 3-m high, 30-m wide, and 0.04-m thick (the wooden vertical poles are 0.1-m thick). The center point of the fence has coordinates 694477.5E, 6175332N (UTM32 WGS32) and is ≈78 m southeast of the Roskilde Fjord coastline. Due to land restrictions and the orientation of the coastline, the fence is oriented ≈42° from the true north (winds from the direction ≈312° are normal to the fence).

The terrain's slope behind the fence was measured with a Trimble global positioning system (GPS), along two lines from its corners. Figure 4-top illustrates the fence experiment and the instrumentation. Figure 4-bottom illustrates the positions where we measured on the vertical plane (described in Sect. 3.3) and the terrain elevation. Note that the reference system is not at the fence center but 1.53 m southwest and so fence corners are not at the same distance from the reference system (see Table 1). The terrain height above the fence base for the positions at which we measured the shelter is provided at http://www.fence.vindenergi.dtu.dk. The relative direction to the fence, θ, is defined positively increasing clockwise.

Figure 3. Photographs of the fence experiment. (Top) overview of the fence and the instrumentation including the lidars and the mast. (Left) solid and (right) porous fence setups

3.2 Meteorological mast

A mast was deployed northeast of the fence and two Metek USA-1 sonic anemometers were placed on booms oriented towards the fence at 6 and 12 m above the ground and recorded time series of the three wind-speed components and temperature at 20 Hz. Mean and turbulence statistics are estimated over 10-min periods from the sonic anemometer measurements (we also analyze the sonic anemometer time series in shorter time periods as described in Sect. 4). The sonic anemometer times series are linearly detrended over the 10-min period, and mean and turbulence quantities like u_* and L are estimated from the 10-

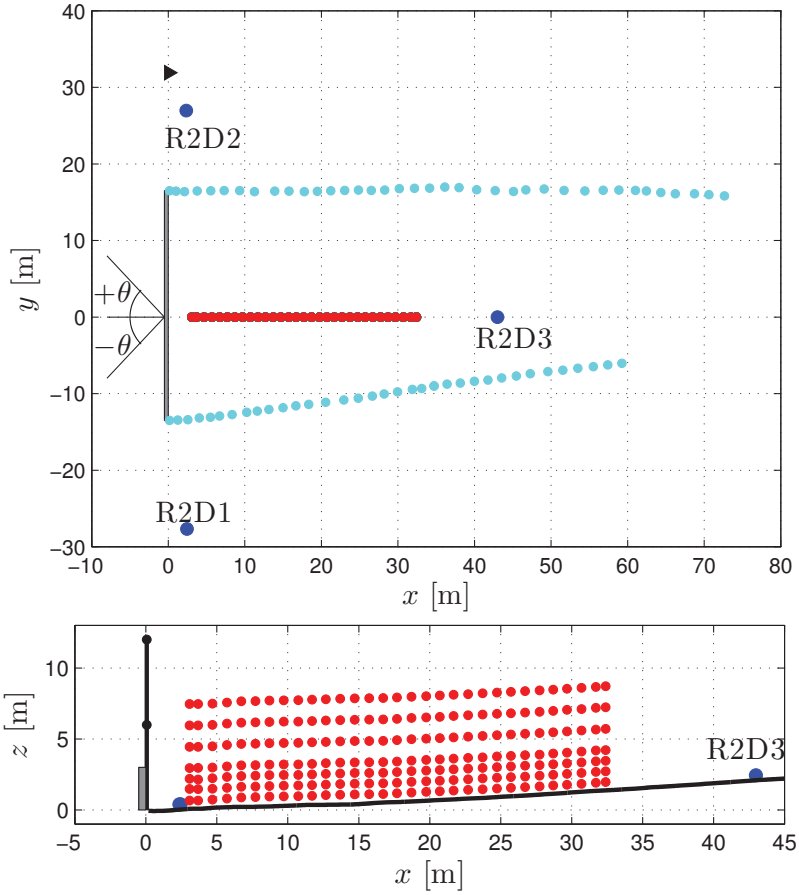

Figure 4. The fence experiment in the reference coordinate system. The positions of the fence (gray rectangle), the lidars (blue circles), the mast (black triangle and black thick line), scanning grid (red circles), and GPS measurements (cyan circles) are also illustrated both at the top (top) and side (bottom) views. The terrain elevation is also shown in the side view

min statistics. The terms T and $\overline{w'T'_v}$ in Eq. (3) are estimated from the sonic anemometer measurements of temperature and kinematic heat flux, respectively. For the latter, we use the crosswind corrections of Liu et al. (2001).

3.3 Lidar measurements

3.3.1 Basics

The three velocity components on the vertical plane were measured using three short-range lidars that were synchronized both in time and space. These three devices comprise the WS. The instruments are based on a continuous-wave (CW) coherent lidar (Karlsson et al., 2000), which is capable of measuring the radial (or line-of-sight) speed and its sign (Sjöholm et al., 2014). The

minimum and maximum measurement ranges and absolute detectable speeds of the WS's lidars are 8 and 150 m[1], and ≈0.15 and 18 m s^{-1}, respectively.

Radial speeds are acquired by a CW lidar within a probe volume, whose dimensions are defined by twice the Rayleigh length and the laser beam's cross-section. The Rayleigh length describes the distribution of the laser intensity along the line-of-sight at a given focus distance and increases quadratically with distance (Sonnenschein and Horrigan, 1971). In the scanning pattern used in the experiment, focus distances varied between 10 and 42 m, corresponding to Rayleigh lengths of 0.10 and 1.52 m, respectively. The cross-section of the probe volume is defined by the waist of the laser beam, which is estimated to be in the order of milimeters.

3.3.2 WindScanner simulation

An optimized positioning of the lidars is a compromise between the size of the scanned area, the error in wind speed (which increases with the size of the scanned area), and the wind-speed components (which we are most interested in accurately measuring). As one lidar measures the line-of-sight velocity only, we need to deploy at least one as far downwind as possible, so that under 'experimentally-ideal' inflow conditions ($\theta \approx 0^\circ$) this unit measures most of the u-component, and as close to the fence to avoid interference of the fence with the probe volume.

A CFD solver of the RANS equations (EllipSys) (Sørensen, 2003) with a standard k-ε model was used to simulate the flow behind the fence (the solid setup only) and the CFD results were used to 'simulate' the flow field observed by the WS including the effect of the probe volume. The CFD simulation was performed using flat terrain with $h/z_o = 300$. A logarithmic profile in balance with the ground roughness was used as inlet condition for $\theta = 0^\circ$. To correctly model the high near-fence velocity gradients, the CFD grid had a 0.03-m wall resolution, which was coarsened with distance to the wall. CFD results were extracted from the same vertical plane as scanned by the WS.

Figure 5 shows both the CFD and the WS's simulated flow assuming that the CFD results 'follow' the terrain elevation. The largest differences for the u-component occur close to the fence and at $z/h = 1.50$ but the relative error is highest for the vertical levels close to the ground. Similarly for w, the difference generally increases the closer to the fence and is highest at the two first vertical levels. These are the areas where the CFD simulation results show the highest w-gradients and so we expect to have large uncertainty in the w-measurements by the WS. A number of positions were tested and the one shown in Fig. 4 and Table 1 was selected because it gave the lowest error for both the u- and w-components 'simulated' by the WS when compared to the CFD results.

3.3.3 Experimental details

The scanning pattern on the vertical plane was decided based on the CFD simulation results and the regions where we are interested in measuring the shelter; we want to measure in both the near- and far-wake regions, and below and above h (up to $z/h \approx 2.5$). The WS's lidars were therefore set to synchronously scan from a position 1 m downwind the fence up to a distance of 10 h and at 7 different levels following the terrain elevation. The lidars were continuously acquiring line-of-sight velocity

[1] limitations imposed by the hardware design and size of the probe volume

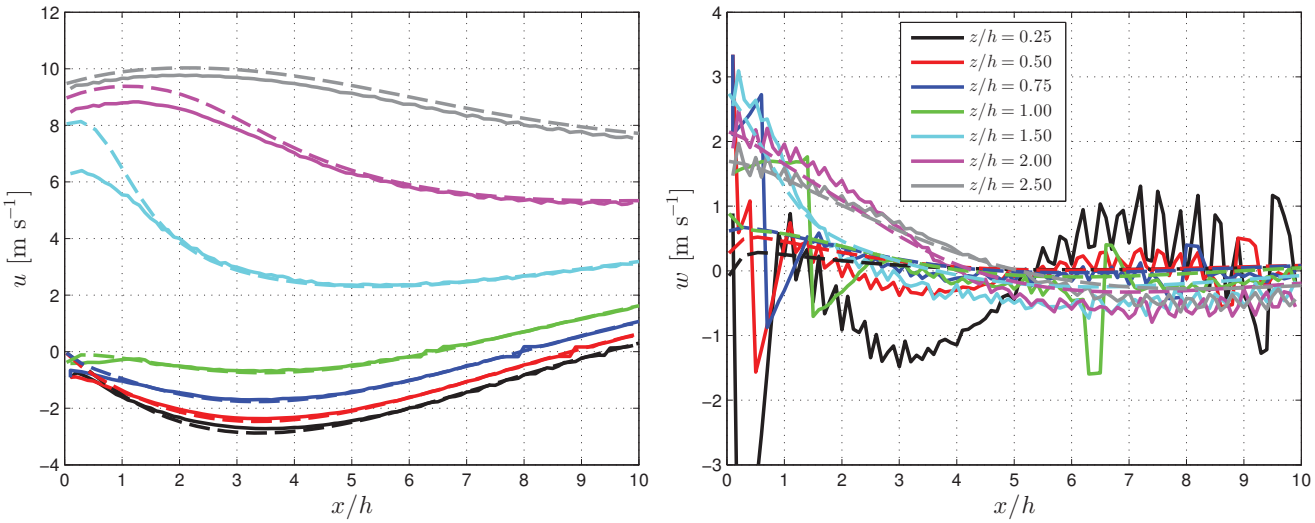

Figure 5. Simulation of the WS measurements (solid lines) and the CFD simulation results (dashed lines) for the u- (left frame) and w-components (right frame) and several vertical levels

Table 1. Instrumentation coordinates for the fence experiment

Instrument	x [m]	y [m]	z [m]
R2D1	2.43	-27.67	0.40
R2D2	2.36	26.96	0.40
R2D3	43.00	0	2.43
Sonic anemometer	0.06	31.91	6, 12
Fence (southern corner)	0	-13.51	0, 3
Fence (northern corner)	0	16.53	0, 3

spectra at ≈49 Hz. The spectra are gridded in 1-m cells and spatially averaged in each cell leading to 31 space- and time-averaged spectra per line. The final scanning grid has thus 31×7 points in the x-z plane. The 7 vertical levels are at the heights $[0.21, 0.46, 0.71, 0.96, 1.46, 1.96, 2.46]\,h$. The 31 positions along the x-axis are given at http://www.fence.vindenergi.dtu.dk.

A 'full-scan' (a complete measurement of all 217 grid positions), took for most days of the campaign ≈21 s. During the second period of the campaign, one lidar had problems with the focus mechanism and to increase the amount of full-scans, we redefine the full-scan on a smaller grid of 29×7 points, i.e. excluding the grid points furthest and closest to the fence.

After the line-of-sight spectra are averaged in each cell, a series of post-processing steps are performed to first remove noise signals and, subsequently, a median frequency estimator is applied to derive the line-of-sight velocity in each spectrum as in Angelou et al. (2012). As the minimum detectable speed of the WS is ≈0.15 m s^{-1}, the WS reports a zero line-of-sight velocity

for velocities lower than this value. We filter out full-scans where line-of-sight velocities are zero or appear as peaks in the time series (for the latter using the method by Goring and Nikora, 2002) for each lidar and grid position.

The u-, v-, and w-components are estimated at each grid position from the scan geometry combined with the line-of-sight velocities. A preliminary analysis of the estimations of w at the first two vertical levels shows unrealistic values because the line-of-sight of the lidars is almost perpendicular to w. Therefore, for all the positions in these two levels, we use the line-of-sight velocities of R2D1 and R2D3 only, so at these two levels we can only estimate u and v assuming a zero w-component.

The WS was mostly operated when the sonic anemometer measurements indicated westerlies and during periods without rain. The WS measurements are thus concentrated on few days as indicated in Table 2, which shows the amount of full-scans per day.

Table 2. Number of full-scans per day by the WS and the fence porosity

Date	No. of full-scans	porosity
March 10	637	solid
March 11	712	solid
March 20	11	solid
March 26	84	solid
March 27	81	solid
April 01	27	solid
September 30	11	porous
October 01	107	porous
October 02	125	porous

4 Data analysis

4.1 Sonic anemometer-lidar intercomparison

Besides the 10-min mean and turbulence sonic anemometer statistics, we derive another set of statistics based on the time period that the WS takes to complete each full-scan (denoted by a $\tilde{}$ symbol). Thus, we also know both the mean wind speed and direction, and their variability, within this shorter period.

The grid point closest to the sonic anemometer at 6 m is at a height of ≈6 m. We compare the WS measurements at this grid position with those from the 6-m sonic anemometer. This is not a fair comparison because the measurements from the WS at each grid position are nearly 'instantaneous', i.e. it takes less than 0.1 s to scan each grid point (we use a $\hat{}$ symbol to refer to them), whereas we use the full-scan period for the sonic anemometer measurements. However, the comparison show us the conditions in which the flow at both positions is similar. Fig. 6 shows a scatter plot of such measurements for both periods of the campaign.

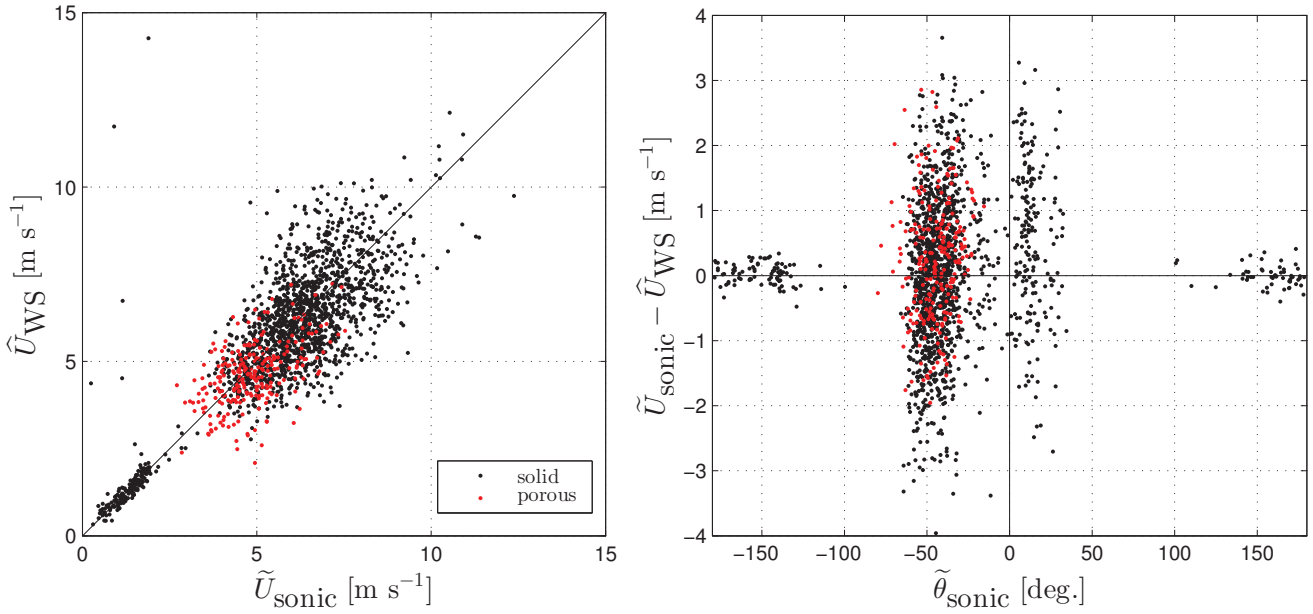

Figure 6. (Left) scatter plot of wind-speed measurements from the 6-m sonic anemometer and the WS for the grid point closest to the fence and at a height of ≈6 m. (Right) the difference between these two measurements as function of the relative wind direction observed by the 6-m sonic anemometer

Figure 6-left illustrates the good agreement between the 6-m sonic anemometer and the WS for the horizontal wind-speed magnitude; the scatter is low and high for low and high wind speeds, respectively. Figure 6-right shows that the degree of scatter is a function of the relative wind direction; when the WS measures downwind the fence ($|\widetilde{\theta}_{\mathrm{sonic}}| \leq 90°$), the scatter is much higher than that for upwind conditions. Although the grid point used is ≈1 h above and ≈1 h downwind the fence, there seems to be a strong effect of the fence on the flow at this position, whereas the effect is nearly negligible for $|\widetilde{\theta}_{\mathrm{sonic}}| \geq 90°$. A similar analysis for downwind conditions using the grid point furthest away from the fence (≈32 m) and at the same vertical level shows a reduction of the scatter (not shown) as the shelter is low there (see Sect. 5). Figure 6-right also shows that most of the measurements are concentrated at $\widetilde{\theta}_{\mathrm{sonic}} \approx -50°$ and that few winds are normal to the fence.

4.2 Inflow conditions

The flow at the mast position (assumed to be undisturbed by the fence for $-75 \leq \theta \leq 75°$) determines the inflow conditions required to estimate the wind-speed ratio due to shelter. Therefore, we need to estimate the surface conditions as a function of relative wind directions at the site.

Assuming homogenous inflow over flat terrain, we estimate z_o from Eq. (1) using 10-min mean and turbulence sonic anemometer statistics. Thus, we have two z_o-values derived using either sonic anemometer for each 10-min period. To compute ψ_m, we use the forms in Peña (2009). Table 3 shows the median of such z_o-estimations based on the 6- and 12-m sonic

anemometers for March and September 2015 and for 10° θ-intervals (we use the 10-min mean sonic anemometer wind direction $\overline{\theta}_{\text{sonic}}$ to classify the 10-min sonic anemometer statistics into relative direction intervals). As shown, for both periods, z_o increases with increasing $|\theta|$, as expected, due to the topography upstream the fence (see Fig. 2). Further, the difference in z_o-values between both periods is relatively small indicating that, particularly at $\theta \approx 0^\circ$, z_o is greatly influenced by the fjord's surface conditions.

Table 3. Roughness length z_o as function of the relative wind direction θ based on either the 6- or the 12-m sonic anemometer for both March and September 2015. The amount of 10-min samples is also shown

	March			September		
$\theta \pm 5^\circ$	6-m z_o [m]	12-m z_o [m]	No. of 10-min samples	6-m z_o [m]	12-m z_o [m]	No. of 10-min samples
-90	0.0673	0.0785	176	0.0549	0.1204	184
-80	0.0435	0.0542	174	0.0280	0.0574	193
-70	0.0231	0.0173	174	0.0095	0.0143	155
-60	0.0095	0.0070	116	0.0072	0.0089	95
-50	0.0069	0.0095	114	0.0052	0.0068	79
-40	0.0049	0.0075	148	0.0028	0.0048	120
-30	0.0031	0.0051	183	0.0012	0.0024	108
-20	0.0031	0.0036	61	0.0009	0.0014	70
-10	0.0021	0.0033	40	0.0004	0.0005	74
0	0.0014	0.0010	33	0.0009	0.0018	118
10	0.0013	0.0026	61	0.0018	0.0064	140
20	0.0014	0.0051	15	0.0030	0.0046	106
30	0.0015	0.0043	43	0.0060	0.0084	93
40	0.0020	0.0038	16	0.0121	0.0077	47
50	0.0113	0.0447	10	0.0407	0.0536	15
60	0.0280	0.0859	12	0.0975	0.2840	11
70	0.0204	0.0778	34	0.0172	0.0641	1
80	0.0149	0.0970	55	0.0151	0.1155	10
90	0.0330	0.2586	73	0.0289	0.3818	7

We need to find out if it is sufficient to describe the inflow using Eq. (1) with the z_o-values in Table 3 given that the terrain is not flat, the upstream conditions not homogeneous, and the atmospheric conditions generally not neutral. For this, we define 'case' studies based on θ-intervals and we select the data, which are included in each case, using the full-scan mean direction from the 6-m sonic anemometer, i.e. $\widetilde{\theta}_{\text{sonic}}$ (see Table 4).

Table 4. Case studies for a number of θ-intervals. Refer to the text for details

Case	Porosity	θ [deg.]	$\langle z_o \rangle$ [m]	$u_{*\text{est}}$ [m s^{-1}]	$\langle z/L \rangle$	No. of full-scans
I	solid	0 ± 15	0.0016	0.36	0.021	159
II	solid	0 ± 30	0.0019	0.36	0.015	304
III	solid	-30 ± 15	0.0037	0.34	0.023	604
IV	solid	-60 ± 15	0.0131	0.39	0.045	583
V	solid	30 ± 15	0.0016	0.35	0.007	62
VI	solid	0 ± 30	0.0019	0.28, 0.27	0.044	92
VII	porous	-30 ± 15	0.0016	0.25	-0.068	128

The case studies are selected so that each has a significant number of full-scans and that we can study the influence on the shelter of a wider θ-interval (cases I and II), θ itself (cases I and III–V), atmospheric stability (cases II and VI), and porosity (case VII). Table 4 provides an estimation of different parameters that are used to reproduce the inflow conditions for each case, which are also illustrated in Fig. 7-left. For each case, we:

1. ensemble-average the z_o-values in Table 3 within the θ-interval in Table 4 (we denote ensemble averages with the $\langle\rangle$ symbol),

2. estimate a 'new' friction velocity $u_{*\text{est}}$ with Eq. (1) assuming $\psi_m(z/L) = 0$ and using the sonic anemometer wind-speed measurement at 6 m, ensemble-averaged from the sonic anemometer mean wind speeds within the full-scan period,

$$u_{*\text{est}} = \frac{\kappa \, \langle \widetilde{U} \rangle_{\text{sonic}}}{\ln\left(6 \text{ m} / \langle z_o \rangle\right)}, \tag{10}$$

3. estimate the 'mean' inflow wind profile $\langle U_o(z) \rangle$[2] using Eq. (1) assuming $\psi_m(z/L) = 0$ (solid color lines in Fig. 7-left) as

$$\langle U_o(z) \rangle = \frac{u_{*\text{est}}}{\kappa} \ln\left(\frac{z}{\langle z_o \rangle}\right). \tag{11}$$

As shown, the estimations of the inflow profiles are in good agreement with the sonic anemometer measurements (an absolute error of 0.18 m s^{-1} is computed at 12 m for case V as the largest of all cases). We therefore assume that, although present, the topographic effects at the mast position within the heights 6–12 m can be neglected for these θ-ranges. The inflow is thus well described by the logarithmic profile.

In addition, Fig. 7-left shows three more profiles for case I. The black dashed line shows the mean inflow conditions but using the ensemble-average u_* of u_*-values estimated from the 6-m sonic anemometer with Eq. (2) within the full-scan period, i.e. $\langle \widetilde{u_*} \rangle$. In this case, there is a systematic underestimation of the inflow wind speed because $\langle \widetilde{u_*} \rangle$ is about 13% lower than $u_{*\text{est}}$ (the latter is given in Table 4). The results in the black dash-dotted line are obtained similarly to those in the solid lines

[2]Although this is not an ensemble average per definition, we use the $\langle\rangle$ symbol because it results from the ensemble-averaged roughness length $\langle z_o \rangle$

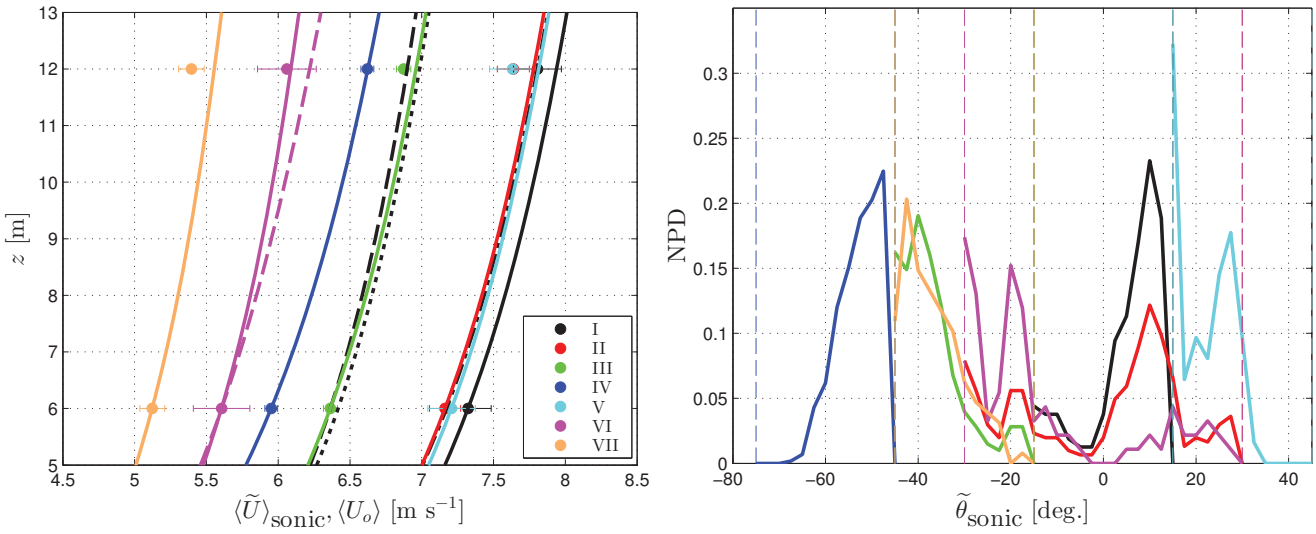

Figure 7. (Left) Inflow conditions for the case studies. The circle markers indicate the ensemble-averaged sonic anemometer measurements $\langle\widetilde{U}\rangle_{\text{sonic}}$ ($\pm$ the standard error in the error bar) and the lines the estimations of the mean inflow conditions $\langle U_o(z)\rangle$ (see text for details). (Right) normalized distribution (NPD) of the relative wind direction from the 6-m sonic anemometer $\widetilde{\theta}_{\text{sonic}}$ for the case studies

but using the 12-m sonic anemometer and the $\langle z_o\rangle$ derived from the observations at that height. Therefore, the estimated inflow wind speed at 12 m is equal to the ensemble-average sonic anemometer wind speed at the same height. The results in the black dotted line are found with the same methodology as that used for the results in the dashed line but with the 12-m sonic anemometer. From these three results, we confirm: first, that turbulent fluxes estimated in the short period of the full-scan are not adequate for deriving the inflow conditions (see the work of Lenschow et al., 1994) and, second, that similar results are obtained when using z_o-estimations based on either the 6- or 12-m sonic anemometer. This also gives us an idea of the small effect that the internal boundary layer (developed at the coastline) has on the inflow profile at the mast position and within the heights between the sonic anemometers.

For case VI, a second mean inflow profile (magenta dashed line) is shown in Fig. 7-left. Case VI is similar to case II but we narrow the analysis to stable conditions $z/L \geq 0.01$ from the 'concurrent'[3] 10-min derived turbulence sonic anemometer estimates at 6 m. $u_{*\text{est}}$ can be computed as in Eq. (10) and, in addition, the correction due to atmospheric stability can be included (the result is the second value for the $u_{*\text{est}}$ column in Table 4). Thus, the magenta dashed line shows the mean inflow profile using Eq. (11) with this new $u_{*\text{est}}$ value, which overestimates the mean wind speed at 12 m by 0.16 m s^{-1} only.

For each case in Table 4, we include the average dimensionless stability $\langle z/L\rangle$-value, which is found by ensemble-averaging the 10-min turbulence fluxes from the 6-m sonic anemometer that are 'concurrent' with the time of the full-scans. As shown, the atmosphere for the 'solid fence' cases is in average stable, except for case V, which corresponds to the most northern

[3]Quotation marks because a full-scan takes less than 10 min

winds, and for the 'porous fence' case the atmosphere is unstable. Interestingly, although we do not narrow the filtering criteria to stable conditions for case IV, $\langle z/L \rangle$ is higher for this case than for case VI.

Figure 7-right shows that the distribution of $\widetilde{\theta}_{\text{sonic}}$-values for each case is not uniform and that the center of the interval, in most cases, differs from the mean of the relative directions within the interval; thus these distributions should be taken into account when evaluating models. We provide the values of such distributions at http://www.fence.vindenergi.dtu.dk.

5 Results

5.1 Wind-speed ratio

We classify the data from the WS's full-scans into the cases in Table 4 using the $\widetilde{\theta}_{\text{sonic}}$-values. The horizontal velocities from the WS are then ensemble-averaged within each case, $\langle \widetilde{U}(z)_{\text{WS}} \rangle$, and the wind-speed ratio is estimated by normalizing these averages by the case-correspondent 'mean' inflow profile (described in Sect. 4.2).

The plots in Fig. 8 illustrate the wind-speed ratio for each case. Although $\widetilde{\theta}_{\text{sonic}}$ is not uniformly distributed within the chosen relative direction intervals, the effect of the fence on the flow for varying θ-values is well observed, particularly from the results between cases I, III and IV (three left frames from the top). Case I, as expected, seems to have the deepest shelter effect of these three cases, which diminishes when increasing $|\theta|$ and, for case IV, the effect of the fence is only noticed for $x/h \lessapprox 3$. For case II, which is defined similar to case I but for a broader θ-interval, the effect of the fence on the flow is smoother and seems slightly deeper than that for case I but the differences are not large. This is most probably due to the concentration of full-scans at $\widetilde{\theta}_{\text{sonic}} \approx 10^\circ$ in both cases. Case VI, the 'stable' case II, also shows a similar behavior but with slightly deeper shelter effects than case II. Case V, similarly defined as case III but with θ centered at 30°, shows reductions up to 50% for $x/h \lessapprox 4$ as case III also does. Case VII, which is comparable to case III but for a different porosity, does not show wind-speed ratios close to zero but the shelter seems to extend further away from the fence.

For cases I–III and VI we notice a small region where the wind-speed ratio is larger than one, located at $x/h \approx 2.5$ and $z/h \approx 2.5$. High wind-speed ratios within the range $1 \leq x/h \leq 4$ are also observed for some of the other cases in Figs. 9–11. These figures illustrate the behavior of the wind-speed ratio but separated into the u- and v-components, with distances downwind the fence, for the seven different levels, and for the seven cases. For $z/h = 2.46$ (Fig. 11), a u-'bump' is clearly visible for all cases where the fence is solid (it is also present on the data of the porous setup). In Fig. 12, we show this high wind-speed ratio from the CFD simulation (used to estimate the WS's error in Sect. 3.3). The CFD simulation was performed over flat terrain without roughness changes and so it is the fence itself that causes the increased vertical velocity shear. Further, the results in Figs. 9–11 for case IV, in which the inflow is the most oblique, show that both u- and v-components do not largely vary for $x/h \geq 7$. This shows us that the effect of the topography on the flow is small at all scan positions on the vertical plane relative to that at the mast position (the wind-speed ratio based on U is $\approx$1).

In Fig. 8, the sign and magnitude of the ensemble-averaged WS's u-component is also illustrated. A region of reverse flow is visible for all cases when the fence is solid; this is also seen on the left frames of Figs. 9–11. This region is also shown in Fig. 12 but for the CFD results it extends much further downwind because the simulation is performed for $\theta = 0^\circ$ only.

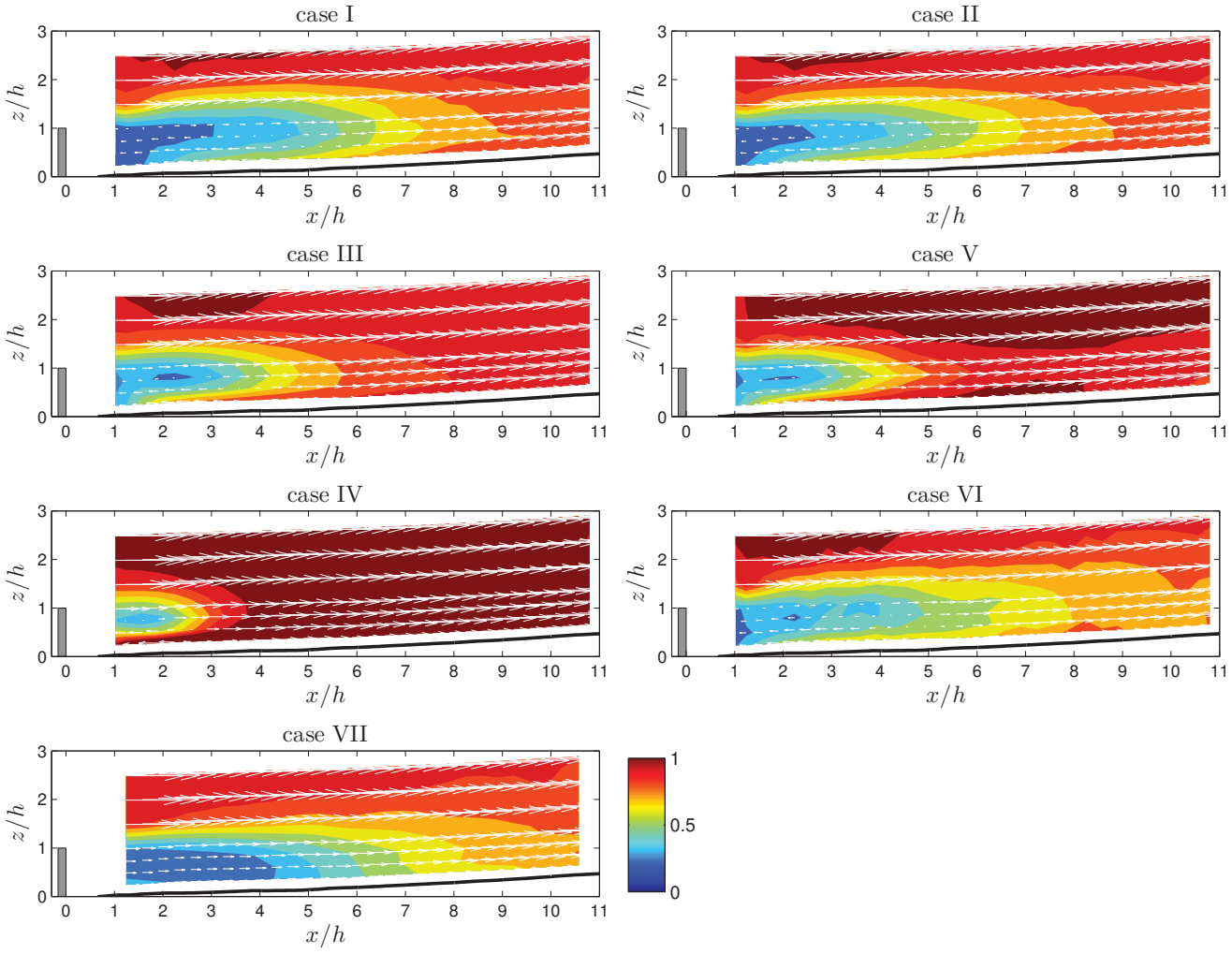

Figure 8. Averaged wind-speed ratio $\langle \widetilde{U}(x,z)_{\mathrm{WS}} \rangle / \langle U_o(z) \rangle$ (colorbar) behind the fence for a number of cases. Vectors indicate the magnitude and sign of the ensemble-averaged u-component

The results in Figs. 9–11 confirm those in Fig. 8; for the solid setup, case VI generally shows the highest shelter in the far wake when looking at the u-component, systematically followed by cases II, I, III, V, and IV, as expected, due to the relative inflow directions, a ranking supported by the proximity of the v-component to zero for each of the cases. Interestingly, the behavior of the u-component for case VII follows that of cases I, II and VI in the far wake, and does not strongly vary below h in the near-wake region; case VII is the only case where the u-component does not change sign, i.e. no reverse flow. For all the other cases, reverse flow can be distinguished and vanishes only at $z/h \geq 0.96$. The behaviour of the u-component with distance from the fence is similar for cases I, II and VI, although the differences in the cases' obliquities are evident when looking at the v-component. It is interesting to note that for the porous case corresponding to oblique flow, at the two

first vertical levels and for $x/h \lessapprox 4$, the horizontal wind vector does not rotate much compared to the inflow condition; the v-component seems to be less effectively reduced compared to the solid cases. For the latter cases the horizontal wind vector strongly rotates downwind of the fence.

Cases III and V show a similar behavior for the u-component; case V systematically showing less shelter, which is explained by the slight higher proximity to zero of the v-component in case III. In both cases, the v-component behaves remarkably similar but with opposite sign at all vertical levels. The average wind-speed ratio for both u- and v-components as function of distance from the fence and for each level and case are presented at http://www.fence.vindenergi.dtu.dk.

5.2 Self-preserving velocity profiles

Using observations from three of the cases in which the θ-interval is center at 0°, we compute the self-preserving forms (Sect. 2) and illustrate them (Fig. 13). We:

1. estimate a 'mean' shear exponent $\langle n \rangle$ using the case-concurrent ensemble-average sonic anemometer measurements and the power law,
$$\langle n \rangle = \frac{\ln\left[\langle \widetilde{U} \rangle_{\text{sonic}}(z = 6\text{ m}) / \langle \widetilde{U} \rangle_{\text{sonic}}(z = 12\text{ m})\right]}{\ln(6\text{ m}/12\text{ m})}, \tag{12}$$
2. compute a 'mean' K using the average roughness (Table 4), $\langle K \rangle = 2\,\kappa^2 / \ln\left(h/\langle z_o \rangle\right)$,
3. use the estimations of the mean inflow (Eq. 11) at the vertical levels and at $z = h$ to compute the average self-similar profiles,
$$\frac{\langle \Delta U(x,z) \rangle}{\langle U_o(h) \rangle}\left(\frac{x}{h}\right) = \frac{\langle U_o(z) \rangle - \langle \widetilde{U}(x,z) \rangle_{\text{WS}}}{\langle U_o(h) \rangle}\left(\frac{x}{h}\right), \tag{13}$$
4. estimate a 'mean' η-value, $\langle \eta \rangle$, based on Eq. (7) using $\langle K \rangle$ and $\langle n \rangle$.

Figure 13 shows the self-preserving profiles for a number of downwind distances; near-wake profiles ($x/h < 5.6$) in grey markers and far-wake profiles ($x/h > 6.24$) in non-grey circles. Equation (8) with $A = 9.75$ is also shown. Further, we fit Eq. (9) to the far-wake profiles, where C_h is estimated in a least-squares sense.

The profiles in the near wake do not generally converge onto each other, whereas those in the far wake do, particularly for cases II and VI with the broad direction interval. Equation (9) with the adjusted C_h agrees better with the profiles compared with Perera's expression in Eq. (8), particularly where the term $[\langle \Delta\, U(x,z) \rangle / \langle U_o(h) \rangle]\,(x/h)$ peaks (vertical levels below h), due to the low C_h. For these cases, Perera's estimations result in a general overestimation of the wind-speed ratio below h.

The adjusted C_h-value in Eq. (9) changes considerably for these cases. For the narrow direction interval (case I), it is nearly half the value recommended by Taylor and Salmon for 2D fences and increases the broader the interval. The increase of C_h in case II compared to case I can be explained by the θ-distribution in Fig. 7-right; the ensemble-average relative direction in case I is 6.27° and in case II is 0.39°, which partly explains the larger effect of the fence on the flow for case II (see also the differences in the v-component in Figs. 9–11). The effect on the flow is larger in case VI; the stable conditions might be responsible for the increase in C_h and the deeper wake but this is also the case where the v-component is closest to zero.

6 Conclusions and discussion

Full-scale flow measurements on a vertical plane behind a fence are presented. The measurements were conducted by the WS and agree well with sonic anemometer measurements from a nearby mast when the wind is not largely disturbed by the fence. Simulation of the WS measurements reveals that the WS tends to underestimate the magnitude of the u-component at $x/h \lessapprox 4$ and $z/h > 1$. This is mostly due to the combination of the high vertical velocity gradient and the large probe volume of the lidar furthest downwind from the fence.

The wind-speed ratio (defined by either u, v, or U with respect to the inflow) depends on the inflow conditions. We assume the topographic effects at each of the positions on the vertical plane to be similar to those at the mast position at the same height, as the wind-speed ratio (based on U) approaches one for the case where the inflow is the most oblique (case IV) at $x/h \gtrapprox 6$ and for all vertical levels. Between the sonic anemometers (6–12 m), the inflow conditions are well described by the logarithmic profile using direction-dependent roughness values estimated from the 10-min sonic anemometer observations. Orographic effects can thus be negligible at the mast (between sonic anemometers) but the effect of the sea-to-land roughness change upwind the fence is perhaps important. Inflow conditions derived from the sonic anemometers are related mostly to the flow characteristics upwind the closest sea-to-land roughness change; the wind profile is in equilibrium with the new surface the first ≈1 m only. When evaluating flow models, topographic effects can be added. We provide the data to derive the inflow conditions that we use to compute the wind-speed ratios and so other inflow conditions can be used if preferred. All data are available at http://www.fence.vindenergi.dtu.dk.

The wind-speed ratio follows the expected behavior; for increasing relative directions and in the far wake, the flow is less disturbed by the fence and within the near-wake region, the porous fence has a lower effect on the flow than the solid fence. For model evaluation, the relative direction distribution needs to be taken into account, as its effects are obvious. We observe a deeper effect of the fence on the flow in the stable compared to the near-neutral case with the same relative-direction interval; model comparison is encouraged to distinguish if this is a result of stability or of the relative-direction distribution. For all cases, the fence decreases the u-component for $z/h \leq 1.5$, and for some cases and levels the fence speeds up the flow.

Direct comparisons with previous experiments are difficult to perform due to differences in, e.g. the nature of the obstacle, the inflow conditions, the accuracy of the measurements, and the shelter regions analyzed. The shelter observations studied by Wilson (2004) for $z/h = 0.5$ and at $x/h = 2$, 4, 6 and 10 for $\theta = 0°$ (with $\varphi = 0.45$) show wind-speed ratios (based on U) of ≈0.48, 0.44, 0.48, and 0.64, respectively, whereas for our porous setup ($\varphi = 0.375$) these are 0.25, 0.27, 0.45, and 0.78, i.e. half the values in the near wake and similar ones in the far wake. It is important to mention that the values in Wilson (2004) are the average of cup-anemometer wind speeds within 1 15-min period only. A more porous windbreak ($\varphi = 0.50$) is studied in Seginer (1975) and the wind-speed ratios for $\theta = 0°$ at $z/h = 0.25$ and $x/h \approx 2.5$, 5, and 7.5 are ≈0.4, 0.3, and 0.35 (for adiabatic conditions), whereas ours (at $z/h = 0.21$) are 0.28, 0.31, and 0.60. They only agree at $x/h = 5$ and the difference at $x/h = 2.5$ is expected due to porosity; Seginer (1975) finds much more reduced shelter with instability in the far wake (our porous case corresponds to an unstable atmosphere). Also important to note is that in both studies the accuracy of the measurements is a major concern. Cup anemometers do not respond well for increasing flow angles and both cup and

sonic anemometers can be subjected to large flow distortion when mounted on masts. We recommend that for future shelter experiments, lidar measurements (which also have inaccuracies) are supplemented by those from cups and sonic anemometers. In our particular case, turbulence is difficult to address with the WS measurements alone as we do not acquire radial velocities at the same grid point for a long-enough period.

The velocity-deficit profiles within the far-wake region ($x/h > 6.24$) converge onto each other, although proper comparison with Counihan et al.'s theory can only be made with a much wider fence. Counihan et al.'s solution agrees better with the self-preserving profiles than Perera's expression, which overestimates the effect of the fence on the flow at $z/h \leq 1$. This is mainly due to the low wake-momentum coefficient when compared to that used for 2D obstacles. Counihan et al. and Perera's works are mostly based on wind-tunnel studies for flow nearly perpendicular to the obstacle. Model evaluation with our measurements could provide insights about accounting for 3D effects on analytical solutions and the wake-momentum coefficient dependency on relative directions.

Acknowledgements. Funding from EUDP, Denmark to both the IEA Task 27 'small turbines in high turbulence sites' and the 'Online WAsP' project (www.mywindturbine.com) are acknowledged.

References

Angelou, N., Abari, F. F., Mann, J., Mikkelsen, T. K., and Sjöholm, M.: Challenges in noise removal from Doppler spectra acquired by a continous-wave lidar, in: Proc. 26th International Laser Rader Conf: Session 5P: Atmosp. winds - turbulence, Porto Heli, 2012.

Castro, I. P. and Robins, A. G.: The flow around a surface-mounted cube in uniform and turbulent streams, J. Fluid Mech., 79, 307–335, 1977.

Counihan, J., Hunt, J. C. R., and Jackson, P. S.: Wakes behind two-dimensional surface obstacles in turbulent boundary layers, J. Fluid Mech., 64, 529–563, 1974.

Goring, D. G. and Nikora, V. I.: Despiking acoustic Doppler velocimeter data, J. Hydraul. Eng., 128, 117–126, 2002.

Gsänger, S. and Pitteloud, J.: Small wind world report 2014, Tech. rep., World Wind Energy Association, Bonn, 2014.

Iaccarino, G., Ooi, A., Durbin, P. A., and Behnia, M.: Reynolds averaged simulation of unsteady separated flow, Int. J. Heat and Fluid Flow, 24, 147–156, 2003.

Karlsson, C. J., Olsson, F., Letalick, D., and Harris, M.: All-fiber multifunction continuous-wave coherent laser radar at 1.55 num for range, speed, vibration, and wind measurements, Appl. Opt., 39, 3716–3726, 2000.

Lenschow, D. H., Mann, J., and Kristensen, L.: How long is long enough when measuring fluxes and other turbulence statistics?, J. Atmos. Oceanic Technol., 11, 661–673, 1994.

Liu, H., Peters, G., and Foken, T.: New equations for sonic temperature variance and buoyancy heat flux with an omnidirectional sonic anemometer, Boundary.-Layer Meteorol., 100, 459–468, 2001.

Mortensen, N. G., Heathfield, D. N., Myllerup, L., Landberg, L., and Rathmann, O.: Getting started with WAsP 9, Tech. Rep. Risø-I-2571(EN), Risø National Laboratory, Roskilde, Denmark, 2007.

Nägeli, W.: Untersuchungen ber die Windverhnisse im Bereich von Schilfrohrwänden, Mitt. Schweiz. Anst. Forstl. Versuchw., 29, 213–266, 1953.

Nord, M.: Shelter effects of vegetation belts – Results of field measurements, Boundary-Layer Meteorol., 54, 363–385, 1991.

Peña, A.: Sensing the wind profile, Tech. Rep. Risø-PhD-45(EN), Risø DTU, 2009.

Perera, M. D. A. E. S.: Shelter behind two-dimensional solid and porous fences, J. Wind Eng. Ind. Aerodyn., 8, 93–104, 1981.

Seginer, I.: Windbreak drag calculated from the horizontal velocity field, Boundary-Layer Meteorol., 3, 87–97, 1972.

Seginer, I.: Atmospheric-stability effect on windbreak shelter and drag, Boundary-Layer Meteorol., 8, 383–400, 1975.

Sjöholm, M., Angelou, N., Hansen, P., Hansen, K. H., Mikkelsen, T., Haga, S., Silgjerd, J. A., and Starsmore, N.: Two-dimensional rotorcraft downwash flow field measurements by lidar-based wind scanners with agile beam steering, J. Atmos. Oceanic Technol., 31, 930–937, 2014.

Sonnenschein, C. M. and Horrigan, F. A.: Signal-to-noise relationships for coaxial systems that heterodyne backscatter from the atmosphere, Appl. Opt., 10, 1600–1604, 1971.

Sørensen, N. N.: General purpose flow solver applied to flow over hills, Tech. Rep. Risø-R-827(EN), Risø National Laboratory, 2003.

Stull, R. B.: An introduction to boundary layer Meteorology, Kluwer Academic Publishers, 1988.

Taylor, P. A. and Salmon, J. R.: A model for the correction of surface wind data for sheltering by upwind obstacles, J. Appl. Meteorol., 32, 1683–1694, 1993.

Wang, H. and Takle, E. S.: On shelter efficiency of shelterbelts in oblique flows, Agric. Forest Meteorol., 81, 95–117, 1996.

Wang, H., Takle, E. S., and Shen, J.: Shelterbelts and windbreaks: Mathematical modeling and computer simulations of turbulent flows, Annu. Rev. Fluid Mech., 33, 549–586, 2001.

Wilson, J. D.: Oblique, stratified winds about a shelter fence. Part I: Measurements, J. Appl. Meteorol., 43, 1149–1167, 2004.

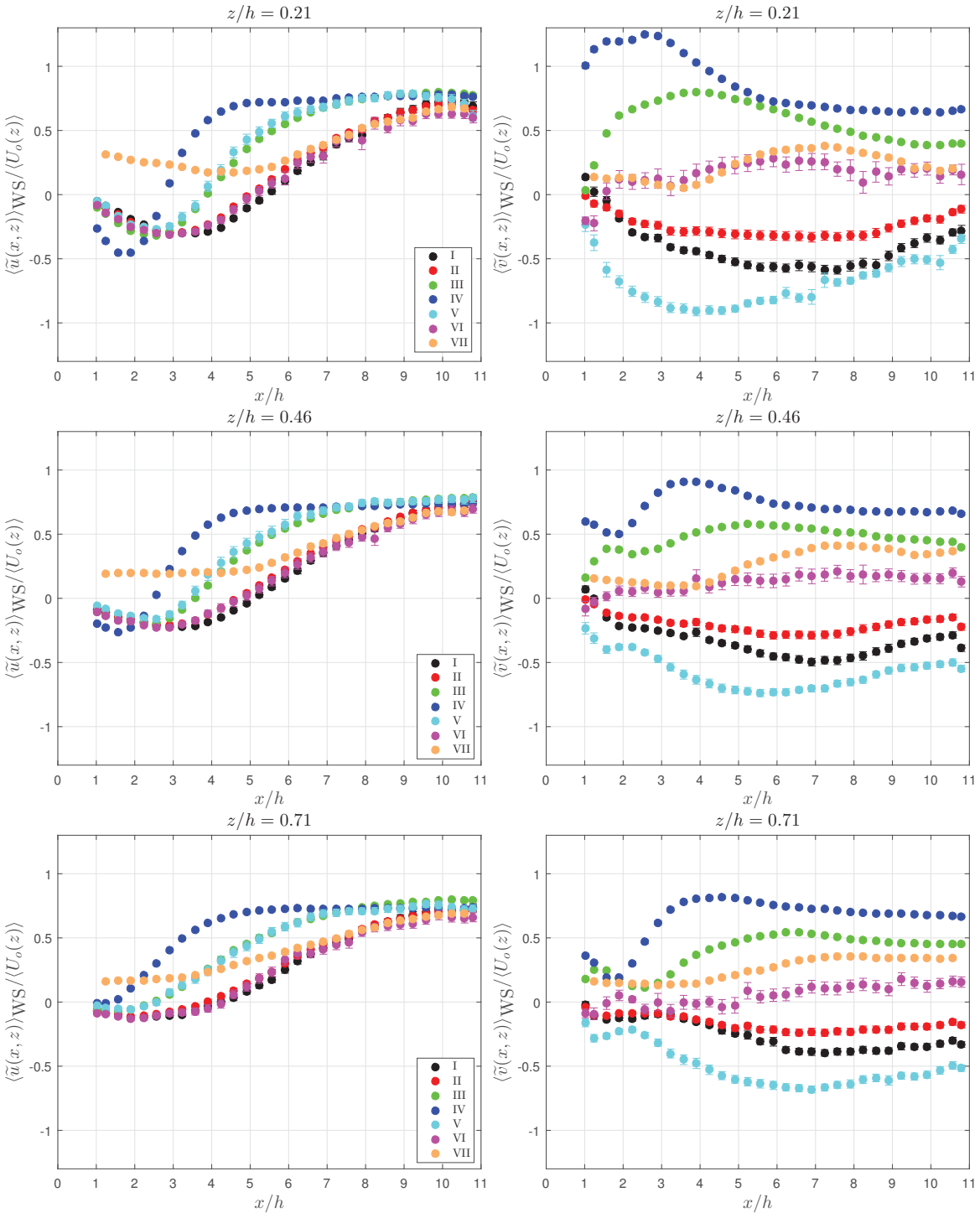

Figure 9. Averaged wind-speed ratio (separated into the u- and v-components) on the first three verticals level behind the fence for a number of cases. $\pm$ the standard error is shown in the error bars

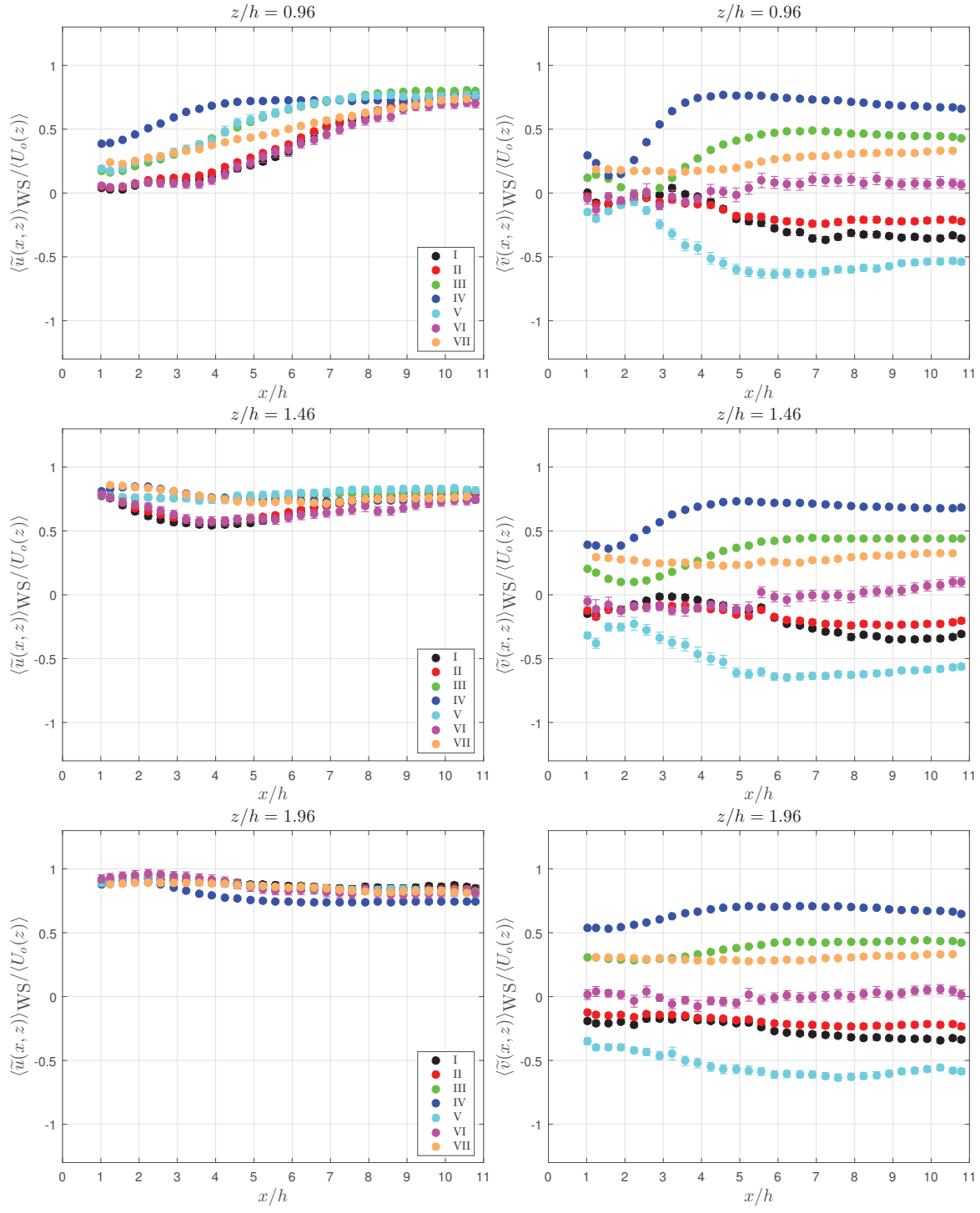

Figure 10. Same as Fig. 9 but for $z/h = 0.96$, 1.46, and 1.96

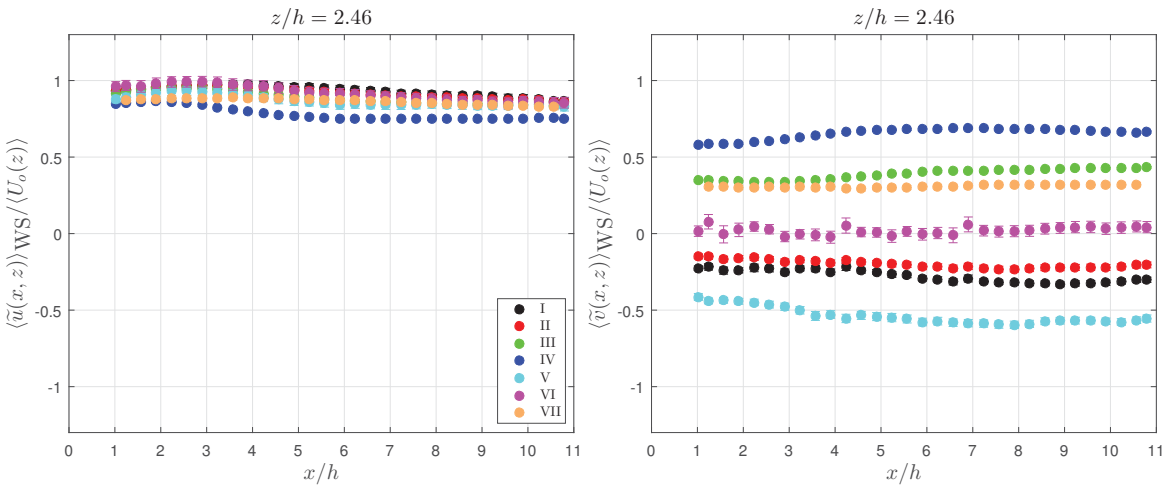

Figure 11. Same as Fig. 9 but for $z/h = 2.46$

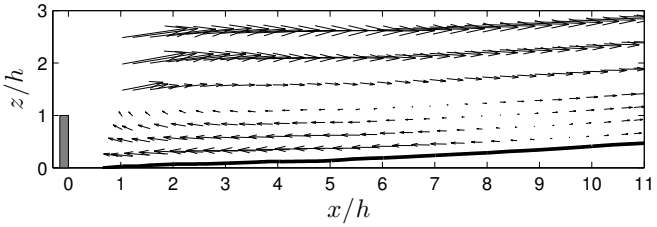

Figure 12. Velocity vector downwind the fence based on the CFD simulation for $\theta = 0^{\circ}$

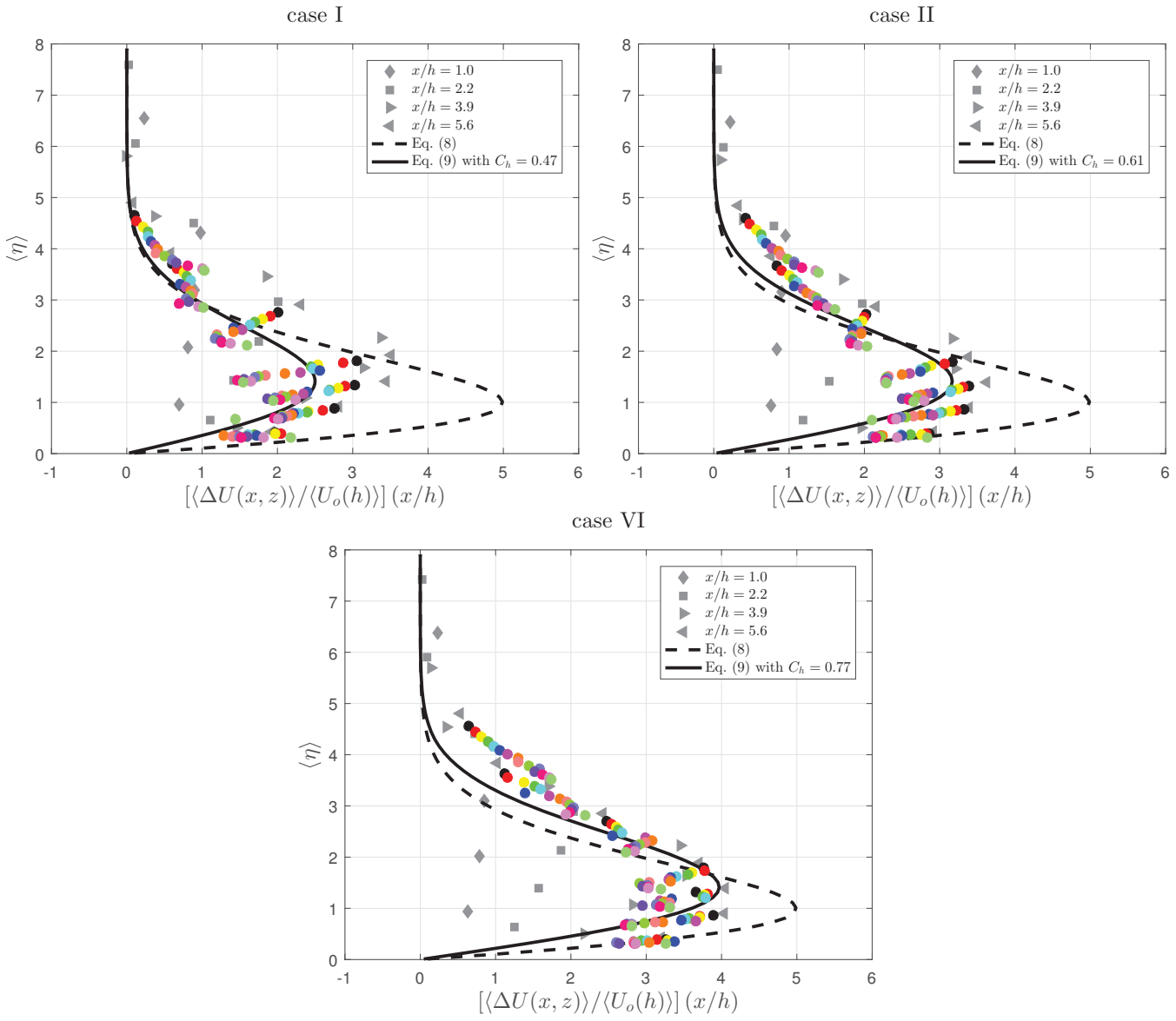

Figure 13. Self-preserving profiles for three cases and a number of downwind distances (details in the text). Results from Eqs. (8) and (9) are also shown